RSC Advances

ROYAL SOCIETY OF CHEMISTRY

www.rsc.org/advances

Journal Name

RSCPublishing

ARTICLE

$NiMoO_4$ nanowire @ MnO_2 nanoflake core/shell hybrid structure aligned on carbon cloth for high-performance supercapacitors

Cite this: DOI: 10.1039/x0xx00000x

Received 00th January 2012,
Accepted 00th January 2012

DOI: 10.1039/x0xx00000x

www.rsc.org/

Di Guo[a], Weiji Ren[a], Zhi Chen[a], Minglei Mao[a], Qiuhong Li[*b], Taihong Wang[**a]

A novel hybrid structure of core/shell $NiMoO_4$@MnO_2 was directly synthesized on carbon cloth by a facile two-step hydrothermal route for supercapacitors. The smart combination of $NiMoO_4$ and MnO_2 hybrid structure shows a synergistic effect for capacitors with greatly enhanced performance. The $NiMoO_4$@MnO_2 electrode yields high-capacitance performance with a high areal capacitance of 3.90 F cm^{-2} at a charge and discharge current density of 8 mA cm^{-2} and 3.22 F cm^{-2} at 24 mA cm^{-2} with a desirable cycling ability (90.5 % of the initial specific capacitance remains after 4000 cycles). Such core/shell hybrid nanoarchitectures exhibit remarkable electrochemical performance with high capacitance and excellent long-term cycling stability, which could be a promising pseudocapacitive electrode material for high-performance supercapacitors.

1 Introduction

Supercapacitors (SCs) have attracted considerable attention in the field of energy storage owing to their high power density, long cycle life and fast charge and discharge rates.[1,2] The unique advantages of SCs are desirable for many applications that require a high energy density and fast charge/discharge rate, such as portable electronics, hybrid electric vehicles and industrial equipment.[3-6] SCs can essentially be classified into two types: electric double layer capacitors (EDLCs) and pseudocapacitors. Pseudocapacitors usually offer much higher specific capacitance and energy density than SCs made of carbon based on double-layer charge storage. Pseudocapacitors fill the gap between the conventional batteries and capacitors in term of electrochemical performances. More analogously to battery, pseudocapacitors stored charges by means of absorption/desorption of ions (Li^+, Na^+, K^+, etc.) and reversible surface/near-surface faradaic reactions.[7-11] Transition metal oxides and hydroxides are the most popular electrode materials of pseudocapacitors in view of their multiple oxidation states for pseudocapacitance generation.[12-18] However, the experimentally obtainable values are often much lower than the theoretical expectations because of inadequate use of entire pseudocapacitive materials and limited electrical conductivity of metal oxides at high rate. Thus, rational design and synthesis of electrode materials with advanced architectures and excellent properties for supercapacitors are a great challenge.

Numerous efforts have been devoted to the synthesis of hybrid electrode materials with the combination of two kinds of materials that enhanced the electrochemical performance. By combining unique properties of individual constituents, enhanced performance has been demonstrated.[11] However, due to the lack of well-defined micro-/nanostructures, the synergistic effect between individual constituents has not worked sufficiently and energy density in most cases is sacrificed.[19] In additon, the limited electron transport can mask the true rate capability of the material.[20] Therefore, the charge storage ability of supercapacitors depends not only on the nature of electrode materials but also greatly on the design of electrode architecture. To improve the ion diffusion kinetics and electron transport at the electrode/electrolyte interface, core/shell hybrid nanostructures directly grown on substrates are well-suited architectures for high-performance supercapacitor electrodes. The "core" with high conductivity, would provide a direct path for the electrons transport and create channels for the effective transport of electrolyte. The "shell" is generally thin layer structure with enlarged surface area, which could shorten ion diffusion path and provide more efficient contacts between the electrolyte ions and active materials for Faradaic energy storage. The disordered nature of the coating material modifies the surface charge to facilitate the adsorption of ion from the electrolyte.[21-23] Meanwhile, the direct growth of nanostructures on conductive substrates avoids the use of polymer binder and conductive additives, substantially reduces the "dead volume" in electrode materials and

facilitates the diffusion of active species and the transport of electrons.[24-29] As a result, reported core/shell hybrid structures on substrates have realized the full potential of the materials in terms of performance.[30-37] For example, hybrid nanostructures of MoO_2@$Co(OH)_2$,[11] Co_3O_4@MnO_2,[19] Co_3O_4@$NiCo_2O_4$[32] and $Ni(OH)_2$@Fe_2O_3[36] have significantly enhanced both the capacitance and durability of electrodes. In these integrated smart architecture, structural features and electroactivities of each component are fully manifested. Despite these achievements, choosing novel suitable electrode materials and their assemblies in appropriate architecture to achieve better performance still remains a challenge due to the complicated synthesis processes.

Herein, we present a facile and scalable strategy to fabricate integrated $NiMoO_4$ nanowire @ MnO_2 nanoflake core/shell hybrid structure aligned on carbon cloth for supercapacitor electrode application. Till now, there is no study on electrochemical performance of the integrated electrodes combining merits of $NiMoO_4$[38-42] and MnO_2[43-49], although the individual capacitive property of both has been extensively investigated. This unique design has following advantages: First, both the core and shell materials are well-known pseudocapacitive metal oxides, which contribute to the overall electrochemical charge storage. Second, the $NiMoO_4$ nanowires (NWs) directly grown on conductive carbon cloth provide a scaffold for the MnO_2 nanoflakes growth, serve as fast electron access for charge storage and delivery, overcoming the limited electrical conductivity of MnO_2 itself to assure an effective electron transport. Third, ultrathin MnO_2 nanoflakes are well wrapped on $NiMoO_4$ NW surfaces, which would enable a fast reversible faradic reaction, reduce the charge-transfer resistance of $NiMoO_4$ and shorten ion diffusion path. Fourth, carbon cloth as a soft substrate manifests incomparable merits for assembled devices since they are low-cost, good electrical conductivity, chemical stability, light weight, flexibility and high porosity. Consequently, in the electrode design, all the desired functions of each constituent are efficiently utilized to realize a strong synergistic effect. The obtained $NiMoO_4$ nanowire @ MnO_2 nanoflake core/shell hybrid structure exhibit large areal capacitance (AC) of 3.90 F cm^{-2} (2294 F g^{-1}) and desirable cycling stability in a 2 M KOH solution.

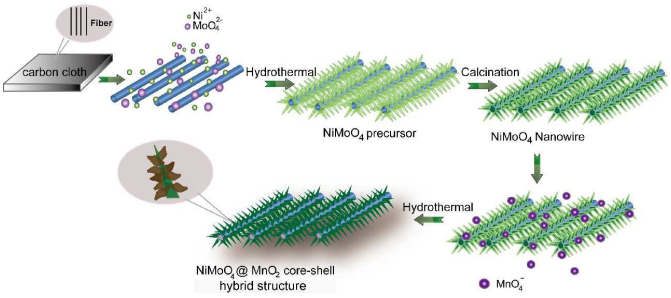

Figure 1 Illustration of the fabrication process of $NiMoO_4$@MnO_2 core/shell hybrid structure.

2 Experimental details

2.1 Synthesis of $NiMoO_4$ @ MnO_2 core/shell hybrid structure on carbon cloth

A commercially available carbon cloth (W0S1002) was used as the supporting material for $NiMoO_4$ @ MnO_2. All the reagents were analytical grade, the nickel nitrate and sodium molybdate were purchased from Tianjin Chemical Reagent Co., potassium permanganate was obtained from Sinopharm Chemical Reagent Co. and used without further purification. $NiMoO_4$ NWs were prepared by a facile hydrothermal synthesis method (150 °C 6h).[38, 41] To fabricate the $NiMoO_4$ NWs coated with thin MnO_2 nanoflakes, a piece of substrate covered with $NiMoO_4$ NWs was first immersed into a 5 mM aqueous $KMnO_4$ solution for 1 h, then placed standing against the wall of a Teflon-lined autoclave. The reaction solution was obtained by mixing 0.01 M of $KMnO_4$ and 0.01 M of Na_2SO_4 in 100 mL of distilled water under constant magnetic stirring and then transferred into Teflon-lined stainless steel autoclave liners. The liner was sealed in a stainless steel autoclave and maintained at 160 °C for 3 h and then cooled down to room temperature. After the reaction was over, the sample was removed and washed by ultrasonication in distilled water followed by acetone for a few minutes in order to remove the residual debris, then dried at 60 °C for 12 h to obtain a $NiMoO_4$@MnO_2 core/shell hybrid structure.

2.2 Characterization

The crystal structure of the samples was characterized with X-Ray diffraction (XRD, Cu Kα irradiation; λ=1.5418 Å) with a SIEMENS D5000 X-ray diffractometer. The morphology and microstructure of the synthesized sample were characterized by a scanning electron microscopy (SEM, Hitachi S4800) and a transmission electron microscope (TEM; JEOL-2010 with an accelerating voltage of 200 kV).

2.3 Electrochemical measurements

The electrochemical measurements were conducted using a three-electrode system in a 2 M KOH aqueous solution. The $NiMoO_4$@MnO_2 hybrid or pristine $NiMoO_4$ NWs (≈ 1×1 cm^2 ; $NiMoO_4$ mass: ≈ 1.1 mg, MnO_2 mass: ≈ 0.6 mg) was directly used as the working electrode. A standard calomel electrode (SCE) was used as the reference electrode and a Pt foil as the counter electrode. The area specific capacitance of the electrode was calculated according to the following equations:

$$C = \frac{i \times t}{\Delta u} \quad (1)$$

where C is the areal capacitance of the electroactive materials, Δu is the potential (V), i is the discharging current density (A cm^{-2} or A g^{-1}) and t is discharge time (s). All the electrochemical experiments were performed on a CHI660e electrochemical workstation (Chenhua, Shanghai).

Electrochemical impedance spectroscopy (EIS) measurements were made with a superimposed 5 mV sinusoidal voltage in a frequency range from 0.01 Hz to 100 kHz at open circuit potential.

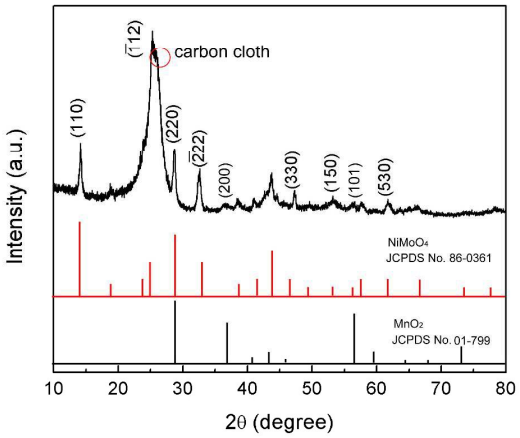

Figure 2 XRD patterns of the $NiMoO_4$@MnO_2 hybrid on carbon cloth.

3 Results and discussion

The electrode of $NiMoO_4$@MnO_2 hybrid structure fabrication process is illustrated in Figure 1. First, a high density of $NiMoO_4$ NWs grown vertically on carbon cloth is obtained via a facile hydrothermal method followed by a calcination process, according to previous work.[41] Typical XRD patterns of the pristine $NiMoO_4$ NWs are distinctly demonstrated in Figure S1. In the second step, $NiMoO_4$ NWs on carbon cloth are immersed into the $KMnO_4$ solution by second hydrothermal reaction to grow thin MnO_2 nanoflakes. The growth of $NiMoO_4$@MnO_2 hybrid can be attributed to "oriented attachment" and "self assembly" processes involving a spontaneous self-organization between neighboring particles to share a common crystallographic orientation. In the process, bonding between the particles reduced overall energy by removing surface energy associated with unsatisfied bonds.[50, 51] In the reaction, $NiMoO_4$ nanowires acted as the 'backbone' to guide the MnO_2 self-assembling growth in aqueous solution without surfactant and stabilizers. Then the 'oriented attachment' can guide the nanoparticles oriented growth. Because of the high surface energy and thermodynamics instability, nanoparticles can attach to the surface of $NiMoO_4$ to decrease surface energy. The crystallographic orientation of the particles with respect to each other is determined by the minimization of the highest surface energy. As shown in Figure 2, the XRD pattern confirms the existence of the $NiMoO_4$ phrase (JCPDF card no. 86-0361) and MnO_2 phrase (JCPDF card no. 01-799). The XRD pattern also includes diffraction peaks corresponding to the carbon cloth substrate. Notably, no impurities have been detected. Figure 3 shows the SEM image of $NiMoO_4$@MnO_2 core/shell hybrid structure aligned on carbon cloth. The low-magnification SEM images in Figure 3a and b indicate the products with high density are uniformly distributed on the fibers of the carbon cloth substrate in a large scale. By contrast, the SEM images of $NiMoO_4$ NWs are displayed in Figure S2. As observed, the $NiMoO_4$ NWs have grown on the carbon cloth support to form net structure. A close SEM examination demonstrates the uniform coverage of MnO_2 nanoflakes on $NiMoO_4$ NW surface (Figure 3c, d). The MnO_2 nanoflake shells are interconnected with each other and almost fully cover the entire $NiMoO_4$ core, forming a net surface morphology. Thus, the core/shell $NiMoO_4$@MnO_2 hybrids are highly accessible to electrolytes for energy storage due to the presence of convenient diffusion channels. Moreover, the robust mechanical adhesion of the hybrid structure is confirmed by an ultrasonication test which shows no material loss occurred after ultrasonication in solution for several minutes. To obtain the cross-section, we scraped off the active materials on the carbon cloth. The cross-sectional SEM image (Figure S3) of $NiMoO_4$@MnO_2 on a carbon fiber shows the thickness of the $NiMoO_4$@MnO_2 layer is about 1.5-2 μm.

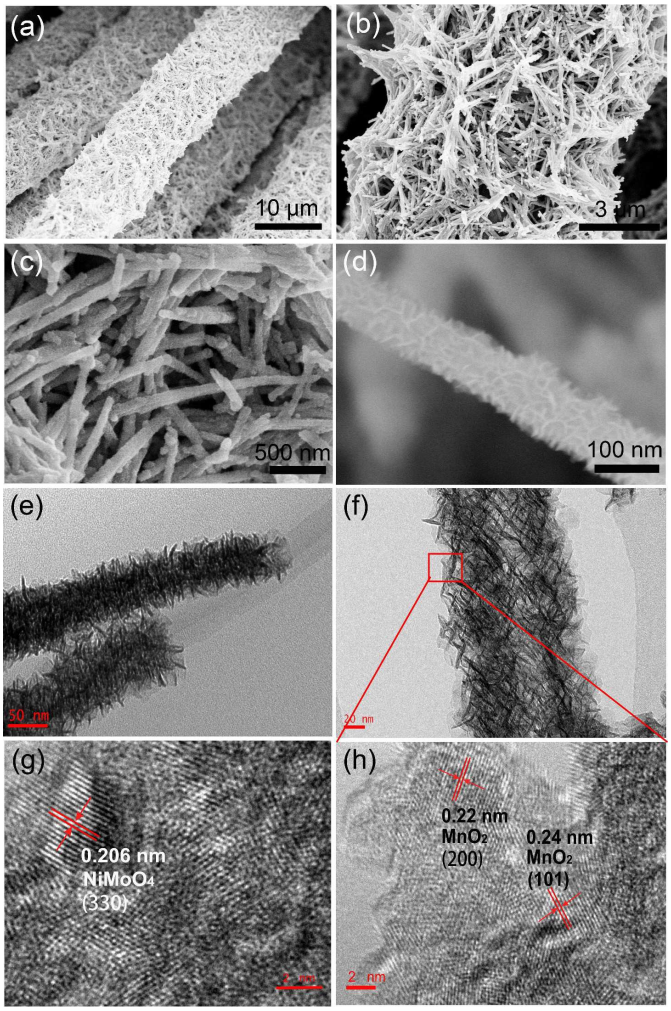

Figure 3 (a-d) Low and high magnification SEM images of the core/shell $NiMoO_4$@MnO_2 hybrid structure on the carbon cloth. TEM micrographs of the samples; (e, f) TEM images of $NiMoO_4$@MnO_2 core/shell hybrid structure scratched from the carbon cloth with synthesized nanostructures; (g)

HRTEM image of pristine $NiMoO_4$ NWs; (h) HRTEM image of MnO_2 nanoflakes.

The structure and morphology of the core/shell hybrid structure was further investigated by TEM. As illustrated in Figure 3e, the pristine $NiMoO_4$ NWs with diameter of 30-60 nm (the TEM image of pristine $NiMoO_4$ NWs is shown in Figure S4) were uniformly covered with ultrathin MnO_2 nanoflakes (< 15 nm). From Figure 3f, it is evidently observed that the $NiMoO_4$ "nanocore" is tightly bonded with MnO_2 nanoflakes, forming a typical core/shell hybrid structure. The high-resolution TEM (HRTEM) image in Figure 3g reveals the interplanar spacing of 0.206 nm, corresponding to the (330) plane of $NiMoO_4$ given in the standard files. The HRTEM measurement was also performed for the MnO_2 nanosheets in red rectangle (Figure 3f). The HRTEM image in Figure 3h shows the interplanar spacing of 0.22 nm and 0.24 nm, which are close to the (200) plane and (101) plane of MnO_2, respectively. Besides, the EDS analysis, shown in Figure S5, demonstrates the presence of Ni, Mo, Mn, O and C elements, arising from the carbon substrate.

To demonstrate the advantage of the hybrid electrode, the cyclicvoltammetry (CV), rate capabilities, cyclic stability studies and electrochemical impedance spectroscopy (EIS) were performed in a three-electrode electrochemical system using SCE as the reference and platinum foil as the counter-electrode. Figure 4a displays the typical CV curves of the $NiMoO_4$@MnO_2 core/shell hybrid electrode (vs. SCE) at different scan rates of 5, 10, 20, 30 and 50 mV s^{-1} in a potential range of -0.2-0.8 V. From the curves, two redox peaks at 0.18 and 0.52 V are clearly observed, which correspond to the reversible reactions of Ni^{2+}/ Ni^{3+} associated with the OH^- ions in the alkaline electrolyte. For comparison, the CV of pristine carbon cloth at 50 mV s^{-1} is shown in in the Supplementary, Figure S6. The capacitance and current of pristine carbon cloth are much lower than $NiMoO_4$@MnO_2 on carbon cloth, which indicated the contribution to capacity from carbon cloth substrate is particularly small. The CV curves of pristine $NiMoO_4$ NWs at 5 mV s^{-1} and 50 mV s^{-1} are also shown in the Supplementary, Figure S7. Obviously, a similar CV shape is still found for the core-shell hybrid, indicating the efficient utilization of the underlying $NiMoO_4$ NWs despite covered by the MnO_2 nanoflakes, while the CV of hybrid array expand obviously and the area integrated within the current-potential curves greatly increases for the core-shell hybrid, leading to a much larger pseudocapacitance. This is mainly due to the great contribution of ultrathin MnO_2 nanoflakes which introduce electrochemical redox reaction to boost the charge storage capability. The CV shape change should certainly be attributed to the presence of MnO_2, which can adsorb cations (K^+) on the electrode surface from electrolyte and suffer from possible intercalation or deintercalation of K^+.[52] The peak current increases almost linearly with the scan rate, suggesting that the rates of electronic and ionic transportation were rapid enough with respect to the scan rates. The shape of the CV curves is not significantly influenced by increasing the scan rate, which indicates improved mass transportation and electron conduction in the host materials.

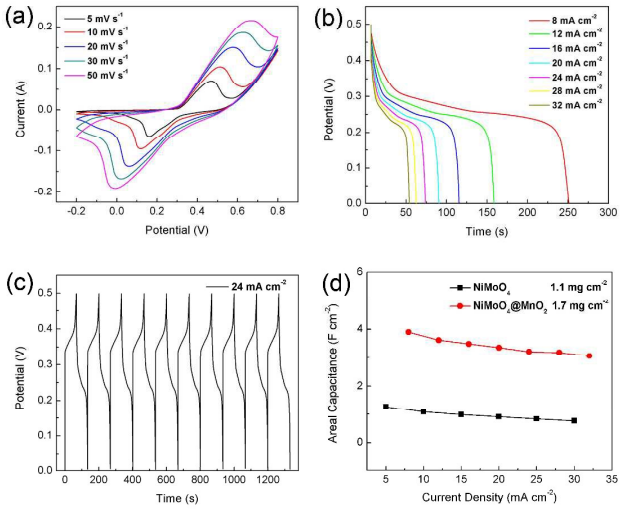

Figure 4 Capacitance properties of the hybrid structure. (a) The CV curves of the $NiMoO_4$@MnO_2 on carbon cloth at different scan rates; (b) Charge-discharge behavior of the hybrid structure on carbon cloth at different current densities; (c) Ten consecutive charge-discharge curves of the hybrid structure at a current density of 24 mA cm^{-2}; (d) Areal capacitance for $NiMoO_4$@MnO_2 hybrid structure and $NiMoO_4$ NWs as a function of the current density.

To further evaluate the performances of the electrode materials, the galvanostatic charge-discharge measurements were performed in the voltage range between 0 and 0.5 V at various current densities. Figure 4b shows the galvanostatic discharge curves at current densities ranging from 8 to 32 mA cm^{-2}. The discharge areal capacitance of $NiMoO_4$@MnO_2 hybrid at 20 mA cm^{-2} was measured to be 3.36 F cm^{-2}, which is higher than the capacitance of pristine $NiMoO_4$ (0.91 F cm^{-2}, shown in the Supplementary, Figure S8). This result directly reveals the advantage of a core/shell hybrid structure pseudocapacitive material for capacitance improvement. The AC of $NiMoO_4$@MnO_2 electrode was calculated from discharge time according to the Eq. (1). Figure 4c exhibits ten consecutive charge-discharge curves of the hybrid structure at a current density of 24 mA cm^{-2}. Figure 4d further illustrates the current density dependence of the areal capacitance of both the hybrid and $NiMoO_4$ NWs. Within the current density from 8 to 32 mA cm^{-2}, the hybrid always delivers a much higher areal capacitance than the $NiMoO_4$ NWs. The $NiMoO_4$@MnO_2 core/shell hybrid electrode delivered high AC values of 3.90, 3.62, 3.49, 3.36, 3.22, 3.19 and 3.07 F cm^{-2} (2294 F g^{-1}, 2053 F g^{-1}, 1976 F g^{-1}, 1894 F g^{-1}, 1876 F g^{-1}, 1806 F g^{-1}) at discharge current densities of 8, 12, 16, 20, 24, 28 and 32 mA cm^{-2} (4.7 A g^{-1}, 7.1 A g^{-1}, 9.4 A g^{-1}, 11.8 A g^{-1}, 14.1 A g^{-1}, 16.5 A g^{-1} and 18.8 A g^{-1}), respectively. The AC gradually decreased with the increase of current density due to the incremental voltage drop and insufficient active material involved in redox reaction at higher current densities. Strikingly, at the highest current

density of 32 mA cm^{-2}, the $NiMoO_4$@MnO_2 still showed a high capacitance of 3.07 F cm^{-2}. Such high AC at large current densities further proves the great advantages of the $NiMoO_4$@MnO_2 hybrid (shown in Figure 5a). The open space between $NiMoO_4$ NWs allows for easy diffusion of the electrolyte into the inner region of electrodes, and the carbon cloth can provide numerous fast electronic transfer channels to improve the electrochemical performance. Furthermore, the directly grown hybrid can ensure good mechanical adhesion and electrical connection to the current collector, avoiding the use of polymer binders and conducting additives, which generally increase the series resistance and the deterioration of capacitance during redox reactions. Compared with single $NiMoO_4$ component, $NiMoO_4$@MnO_2 core/shell hybrid presents many competitive advantages such as rich accessible electroactive sites, short ion transport pathways, superior electron collection efficiency, and even fascinating synergetic properties or multifunctionalities of components. By coating of each $NiMoO_4$ NW with flaky MnO_2, the space between the $NiMoO_4$ NWs is utilized abundantly, which would increase the energy and power per unit area. Moreover, the hybrid nanostructure can effectively decrease the surface energy of the active nanomaterials which may lead to a high level of reversibility. As a result, the AC of $NiMoO_4$@MnO_2 is higher than previously reported core/shell hybrid materials, such as NiO-TiO_2 nanotube arrays (3 F cm^{-2} at 0.4 mA cm^{-2}),[53] Co_3O_4@MnO_2 core/shell nanorod arrays (0.56 F cm^{-2} at 1.25 mA cm^{-2})[19] and $NiCo_2O_4$@MnO_2 core/shell NW arrays (2 F cm^{-2} at 10 mA cm^{-2}).[33] The results imply that $NiMoO_4$@MnO_2 core/shell hybrid could be a promising electrode material for high-performance supercapacitors.

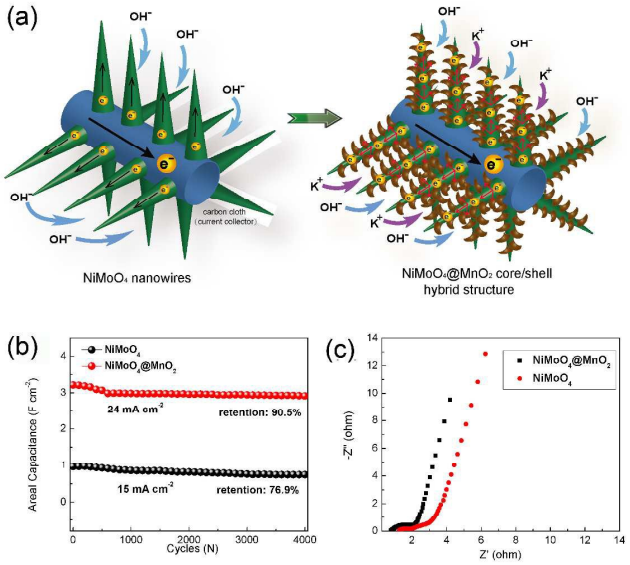

Figure 5 (a) Schematic illustration showing the charge storage advantage of $NiMoO_4$@MnO_2 core/shell hybrid structure, in which both $NiMoO_4$ and MnO_2 provide channels for electron transport. (b) Cycling performance of the $NiMoO_4$@MnO_2 hybrid structure and $NiMoO_4$ NWs; (c) Impedance Nyquist plots of the $NiMoO_4$@MnO_2 hybrid structure and $NiMoO_4$ NWs on carbon cloth at open circuit potential.

The long-term cycling stability of the as-fabricated $NiMoO_4$@MnO_2 core/shell hybrid and pristine $NiMoO_4$ NWs were examined by repeated charge-discharge processes, as shown in Figure 5b. It is clear that both the AC and cycling stability are largely enhanced in the core/shell hybrid electrode. The AC degradation of the core/shell hybrid is estimated to be from 3.22 to 2.92 F cm^{-2} even at a high current density of 24 mA cm^{-2}. The capacitance loss for $NiMoO_4$@MnO_2 core/shell hybrid after 4000 cycles is only 9.5%. By contrast, only 76.9% capacitance was retained (23.1% loss) for a pristine $NiMoO_4$ NWs at current density of 10 mA cm^{-2}. The MnO_2 nanoflakes coated on surface of $NiMoO_4$ NWs improve the electrochemical stability for long cycle life applications at high current densities. Besides, the superior cycling stability can be in part explained by the structural stability of the electrode. After long-term cycling at high current densities, the structural integrity and basic morphology of the $NiMoO_4$@MnO_2 hybrid were overall well preserved with little structural deformation as shown in the Supplementary, Figure S9. In this respect, MnO_2 is proposed to serve as a protecting layer to maintain the $NiMoO_4$ structural integrity during the bulk redox reaction, which would otherwise weaken the nanowire due to the harsh and frequent phase variation. In order to further understand the fundamental behavior of supercapacitor electrodes, EIS analysis was measured and the corresponding Nyquist plots of the two electrodes are shown in Figure 5c. From the plots, we can see that the MnO_2 coating leads to a relatively smaller bulk resistance (R_b), R_b decreased from 1.12 Ω to 0.77 Ω, suggesting the electron conductivity of $NiMoO_4$ NW electrode is improved. Moreover, the semicircle (which corresponds to double layer capacitance C_{dl} and charge-transfer resistance R_{ct}) displays the charge-transfer process at the working electrode-electrolyte interface. The $NiMoO_4$@MnO_2 hybrid also displays lower charge-transfer resistance than pristine $NiMoO_4$ NWs, which is beneficial to the rate capability of the hybrid. The reduced Faraday resistance rendered by the intriguing material combination and the core/shell structure leads to enhanced electrochemical reaction, contributing greatly to high AC of $NiMoO_4$@MnO_2 hybrid. On the other hand, the decreased Warburg impedance (W) represents lower diffusion resistance in $NiMoO_4$@MnO_2 than pristine $NiMoO_4$, which can be attributed to the large surface area of ultrathin MnO_2 nanoflakes which facilitated the diffusion of OH^- to the entrance of $NiMoO_4$ nanocore. The SC performance of the hybrid structure of $NiMoO_4$@MnO_2 and $NiMoO_4$ NWs have been summarized by a radar plot in Figure 6, we can comprehensively evaluate the metrics of as-prepared supercapacitor electrodes, including cycle life, internal resistance, capacitance, etc.[54]

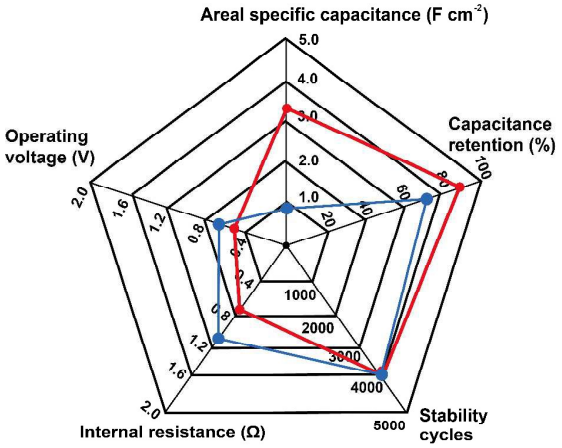

Figure 6 Radar plots to compare the supercapacitor performance of $NiMoO_4$@MnO_2 hybrid structure (red curves) and $NiMoO_4$ NWs (blue curves) on carbon cloth.

4 Conclusions

In summary, this study demonstrated a facile and scalable strategy to construct $NiMoO_4$ nanowire @ MnO_2 nanoflake core/shell hybrid structure aligned on carbon cloth for high-performance supercapacitors. The as-fabricated $NiMoO_4$@MnO_2 core/shell hybrid structure electrode exhibited excellent supercapacitor performance with a high capacitance of 3.07 F cm^{-2} even at 32 mA cm^{-2} and desirable rate performance. Such intriguing capacitive behavior is attributed to the unique core/shell hybrid configuration and the synergistic effects of the combined pseudocapacitive contributions from the $NiMoO_4$ NW core and the ultrathin MnO_2 shell layer. Our work opens up the possibility of constructing high-performance core/shell hybrid materials by self assembly method. The electrode design concept can be readily generalized to other materials and again confirms the feasibility of rational design of 3D hybrid nanostructure electrodes for high-performance supercapacitors.

Acknowledgements

This work was supported by the National Natural Science Foundation of China (Grant No. 21003041, 61376073), Hunan Provincial Natural Science Foundation of China (Grant No. 11JJ7004), Hunan Provincial Innovation Foundation For Postgraduate (Grant No. 521293014) and the Specialized Research Fund for the Doctoral Program of Higher Education of China (Grant No. 20120161110016).

Notes and references

[a] *College of Chemistry and Chemical Engineering, State Key Laboratory of Chem/Bio-Sensing and Chemometrics, Hunan University, Changsha, Hunan 410082, P. R. China. Email: thwang@iphy.ac.cn(T.H. Wang).*

[b] *Pen-Tung Sah Institute of Micro-Nano Science and Technology of Xiamen University, Xiamen, 361005, China. Email: liqiuhong2004@hotmail.com(Q.H. Li).*

Electronic Supplementary Information (ESI) available: [The XRD patterns, SEM and TEM images of $NiMoO_4$ NWs;The EDS patterns of $NiMoO_4$ @ MnO_2 hybrid; CV curves and galvanostatic discharge curves of $NiMoO_4$ NWs; SEM image of the $NiMoO_4$ @ MnO_2 hybrid electrode after 4000 cycles].

1 Y. Zhu, S. Murali, M.D.Stoller, K.J. Ganesh, W. Cai, P. J. Ferreira, A. Pirkle, R.M. Wallace, K. A. Cychosz, M. Thommes, D. Su, E.A. Stach, R.S. Ruoff, *Science*, 2011, **332**, 1537.

2 G. Wang, L. Zhang, J. Zhang, *Chem. Soc. Rev.*, 2012, **41**, 797.

3 M.D. Stoller, R.S. Ruoff, *Energy Environ. Sci.*, 2010, **3**, 1294.

4 W. F. Wei, X. Cui, W. Chen, D.G. Ivey, *Chem. Soc. Rev.*, 2011, **40**, 1697.

5 P. Simon, Y. Gogotsi, *Nat. Mater.*, 2008, **7**, 845.

6 G.H.Yu, X. Xie, Z. N. Bao, Y. Cui, *Nano Energy*, 2013, **2**, 213.

7 J. Jiang, Y.Y. Li, J.P. Liu, X.T. Huang, C.Z. Yuan X.W. Lou, *Adv. Mater.*, 2012, **24**, 5166.

8 P. Simon, Y. Gogotsi, Philos. Trans, *R. Soc. London, Ser. A*, 2010, **368**, 3457.

9 P. Sharma, T.S. Bhatti, *Energy Convers. Manage.*, 2010, 51, 2901.

10 L. Mai, H. Li, L. Xu, X. Xu, Y. Zhao, Y. Luo, Z. Zhang, W. Ke, C. Niu, Q. Zhang, *Sci. Rep.*, 2013, **3**, 1718.

11 K.M. Hercule, Q.L Wei, A.M. Khan, Y.L. Zhao, X.C. Tian, L.Q. Mai, *Nano Lett.*, 2013, **13**, 5685.

12 L.B. Kong, J.W. Lang, M. Liu, Y.C. Luo, L. Kang, *J. Power Sources*, 2009, **194**, 1194.

13 G.P. Xiong, C.Z. Meng, R.G. Reifenberger, P.P. Irazoqui, T.S. Fisher, *Adv. Energy Mater.*, 2014, **4**, 1300515.

14 G.X. Wang, X.P. Shen, J. Horvat, B. Wang, H. Liu, D. Wexler, J. Yao, *J. Phys. Chem. C*, 2009, **113**, 4357.

15 H. Jiang, T. Zhao, C.Z. Li, J. Ma, *J. Mater. Chem.*, 2011, **21**, 3818.

16 M.F. Shao, F.Y. Ning, Y.F. Zhao, J.W. Zhao, M. Wei, D.G. Evans, X. Duan, *Chem. Mater.*, 2012, **24**, 1192.

17 G.P. Xiong, C.Z. Meng, R.G. Reifenberger, P.P. Irazoqui, T.S. Fisher, *Journal of Power Sources*, 2013, **227**, 254.

18 J.P. Liu, J. Jiang, M. Bosman, H.J. Fan, *J. Mater. Chem.*, 2012, **22**, 2419.

19 J.P. Liu, J. Jiang, C.W. Cheng, H.X. Li, J. X. Zhang, H. Gong, H.J. Fan, *Adv. Mater.*, 2011, **23**, 2076.

20 B. Kang, G. Ceder, *Nature*, 2009, **458**, 190.

21 J. Yan, E. Khoo, A. Sumboja, P.S. Lee, *ACS Nano*, 2010, **4**, 4247.

22 C.K. Chan, H.L. Peng, R.D. Twesten, K. Jarausch, X.F. Zhang, Y. Cui, *Nano Lett.*, 2007, **2**, 490.

23 A.E. Fischer, K.A. Pettigrew, D.R. Rolison, R.M. Stroud, J.W. Long, *Nano Lett.*, 2007, **7**, 281.

24 J. Jayalakshmi, K. Balasubramanian, *Int. J. Electrochem. Sci.*, 2008, **3**, 1196.

25 H. Zhang, X. Yu, P. V. Braun, *Nat. Nanotechnol.*, 2011, **6**, 277.

26 J. Xu, K. Wang, S.Z. Zu, B.H. Han, Z. Wei, *ACS Nano*, 2010, **4**, 5019.

27 C.C. Hu, K.H. Chang, M.C. Lin, Y.T. Wu, *Nano Lett.*, 2006, **6**, 2690.

28 P. Banerjee, I. Perez, L. Henn-Lecordier, S.B. Lee, G.W. Rubloff, *Nat. Nanotechnol.*, 2009, **4**, 292.

29 C.H. Tang, X.S. Yin, H. Gong, *ACS Appl. Mater. Interfaces*, 2013, **5**, 10574.
30 X. Xiao, T.P. Ding, L.Y. Yuan, Y.Q. Shen, Q.Z. Zhong, X.H. Zhang, Y.Z. Cao, B. Hu, T. Zhai, L. Gong, J. Chen, Y.X. Tong, J. Zhou, Z.L. Wang, *Adv. Energy Mater.*, 2012, **2**, 132.
31 C.Q. Shang, S.M. Dong, S. Wang, D.D. Xiao, P.X. Han, X.G. Wang, L. Gu, G.L. Cui, *ACS Nano*, 2013, **7**, 5430.
32 G.H. Zhang, T.H. Wang, X.Z. Yu, H.N. Zhang, H.G. Duan, B.A. Lu, *Nano Energy*, 2013, **2**, 586.
33 L. Yu, G.Q. Zhang, C.Z. Yuan, X.W. Lou, *Chem. Commun.*, 2013, **49**, 137.
34 J. Duay, S.A. Sherrill, Z. Gui, E. Gillette, S.B. Lee, *ACS Nano*, 2013, **7**, 1200.
35 X.H. Xia, J.P. Tu, Y.Q. Zhang, X.L. Wang, C.D. Gu, X.B. Zhao, H.J. Fan, *ACS Nano*, 2012, **6**, 5531.
36 W. Tian, X. Wang, C. Y. Zhi, T.Y. Zhai, D.Q. Liu, C. Zhang, D. Golberg, Y. Bando, *Nano Energy*, 2013, **2**, 754.
37 J. Wang, D.L. Chao, J.L. Liu, L.L. Li, L.F. Lai, J.Y. Lin, Z.X. Shen, *Nano Energy*, 2014, **7**, 151.
38 D. Guo, Y.Z. Luo, X.Z. Yu, Q.H. Lin, T.H. Wang, *Nano Energy*, 2014, **8**, 174.
39 D.P. Cai, D.D. Wang, B. Liu, Y.R. Wang, Y. Liu, L.L. Wang, H. Li, H. Huang, Q.H. Li, T.H. Wang, *ACS Appl. Mater. Interfaces*, 2013, **5**, 12905.
40 S.J. Peng, L.L. Li, H. B. Wu, S. Madhavi, X. W. Lou, *Adv. Energy Mater.*, 2014, 1401172.
41 D. Guo, P. Zhang, H.M. Zhang, X.Z. Yu, J. Zhu, Q.H. Li, T.H. Wang, *J. Mater. Chem. A*, 2013, **1**, 9024.
42 M.C. Liu, L.B. Kong, C. Lu, X.J. Ma, X. M. Li, Y.C. Luo, L. Kang, *J. Mater. Chem. A*, 2013, **1**, 1380.
43 D. Guo, X.Z. Yu, W. Shi, Y.Z. Luo, Q.H. Li, T.H. Wang, *J. Mater. Chem. A*, 2014, **2**, 8833.
44 M. Nakayama, T. Kanaya, R. Inoue, *Electrochem. Commun.*, 2007, **9**, 1154.
45 Z.N. Yu, B. Duong, D. Abbitt, J. Thomas, *Adv. Mater.*, 2013, **24**, 3302.
46 H. Jiang, L.P. Yang, C.Z. Li, C.Y. Yan, P.S. Lee, J. Ma, *Energy Environ. Sci.*, 2011, **4**, 1813.
47 J.H. Kim, K.H. Lee, L.J. Overzet, G.S. Lee, *Nano Lett.*, 2011, **11**, 2611.
48 H. Jiang, J. Ma, C. Z. Li, *J. Mater. Chem.*, 2012, **22**, 16939.
49 C.Z. Wei, H. Pang, B. Zhang, Q.Y. Lu, S. Liang, F. Gao, *Sci. Rep.*, 2013, **3**, 2193.
50 L.Q. Mai, F. Yang, Y.L. Zhao, X. Xu, L. Xu, Y.Z. Luo, *Nature Communication*, 2011, **2**, 381.
51 M. Niederberger, H. Colfen, *Physical Chemistry Chemical Physics*, 2006, **8**, 3271.
52 D. Bélanger, T. Brousse, J.W. Long, *Electrochem. Soc. Interface*, Spring, 2008, 49.
53 J.H. Kim, K. Zhu, Y. Yan, C.L. Perkins, A.J. Frank, *Nano Letters*, 2010, **10**, 4099.
54 G.P. Xiong, C.Z. Meng, R.G. Reifenberger, P.P. Irazoqui, T.S. Fisher, *Electroanalysis*, 2014, **26**, 30.